Online Supplementary Material

Supplementary Figures

Petrogenesis of Fe-Ti-V oxide mineralisation in the Kalka intrusion (Giles Intrusions – Musgrave Province, South Australia)

Adam Abersteiner[1,2,3*], Carl Spandler[2], Benjamin Wade[4]

[1]Institute for Sustainability, Energy and Resources, The University of Adelaide, Adelaide SA-5005, Australia

[2]Department of Earth Sciences, School of Physical Sciences, The University of Adelaide, Adelaide SA-5005, Australia

[3]Department of Geosciences and Geography, Research programme of Geology and Geophysics (GeoHel), University of Helsinki, PO Box 64, FIN-00014, Finland

[4]Adelaide Microscopy, The University of Adelaide, Adelaide, Australia

**Corresponding author: adam.abersteiner@adelaide.edu.au*

Supplementary Figure S1

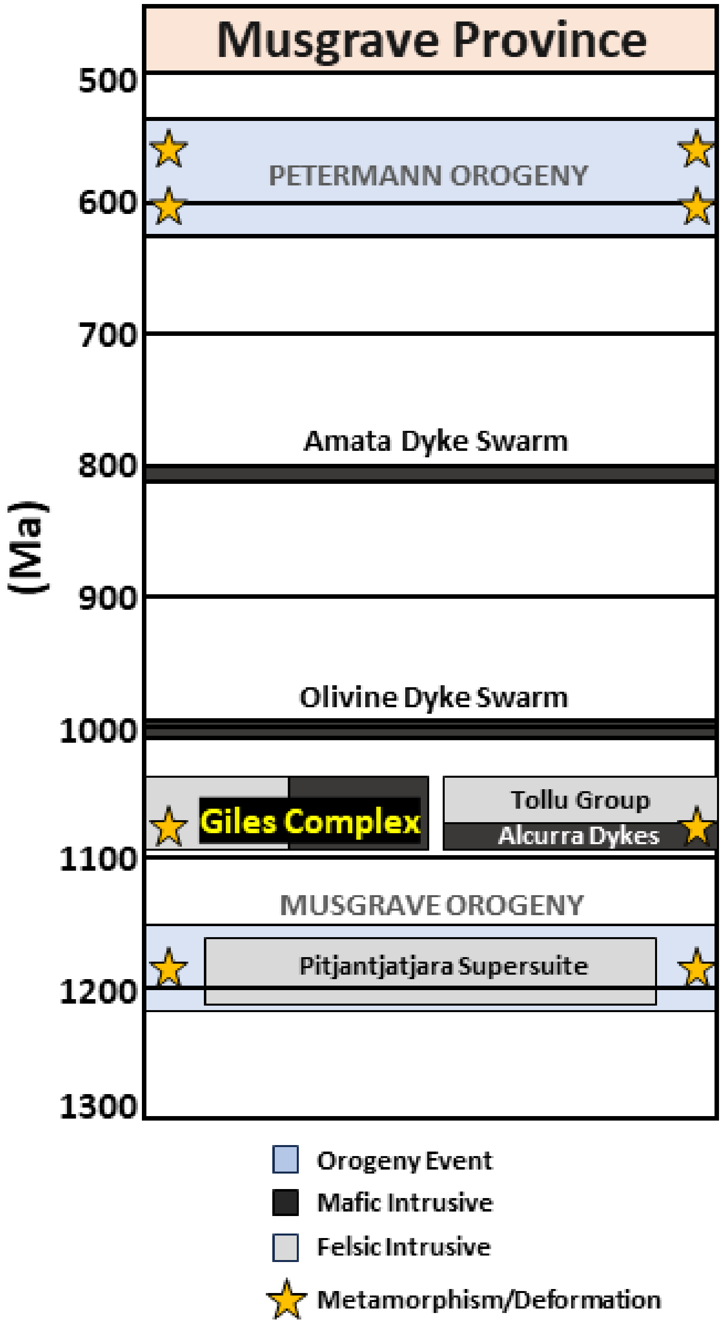

Supplementary Figure S1. Simplified time-space plot (Ma) for the Musgrave Province showing the emplacement of the Giles Intrusions and inferred deformation/metamorphism and orogeny events (modified after Figure 3 of Wade et al., 2008).

Supplementary Figure S2

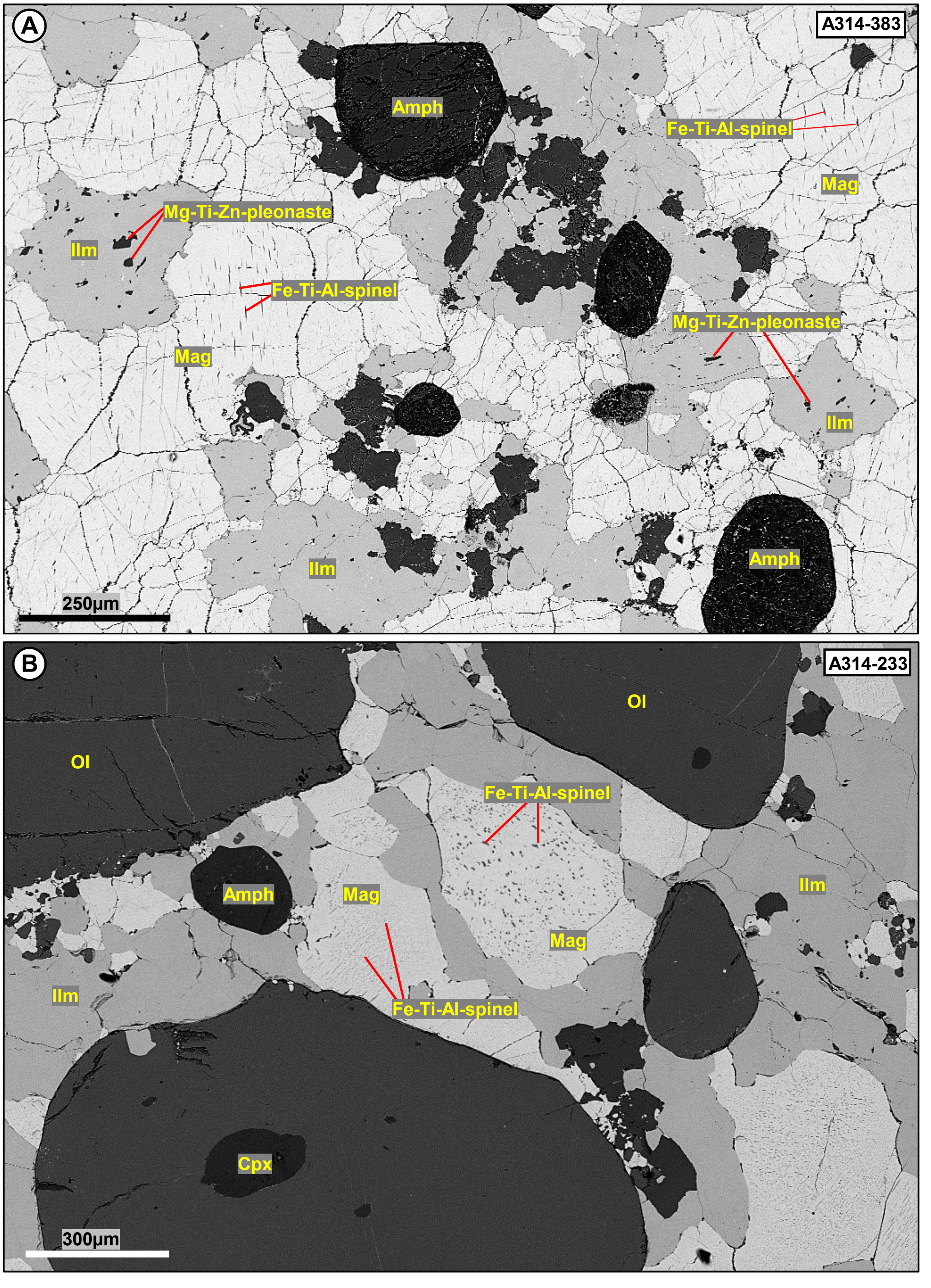

Supplementary Figure S2. Back-scatter electron (BSE) scanning electron microscope (SEM) images of exsolution lamellae of Fe-Ti-Al spinel in magnetite (mag) and Mg-Ti-Zn pleonaste in ilmenite (Ilm) in sample (A) A314-383, and (B) A314-233. The sizes, distribution and abundance of exsolution lamellae varies significantly between different host grains and samples, such as A314-233, where exsolution lamellae is present in magnetite and absent in ilmenite. Ol: olivine, Amph: amphibole, Cpx: clinopyroxene.

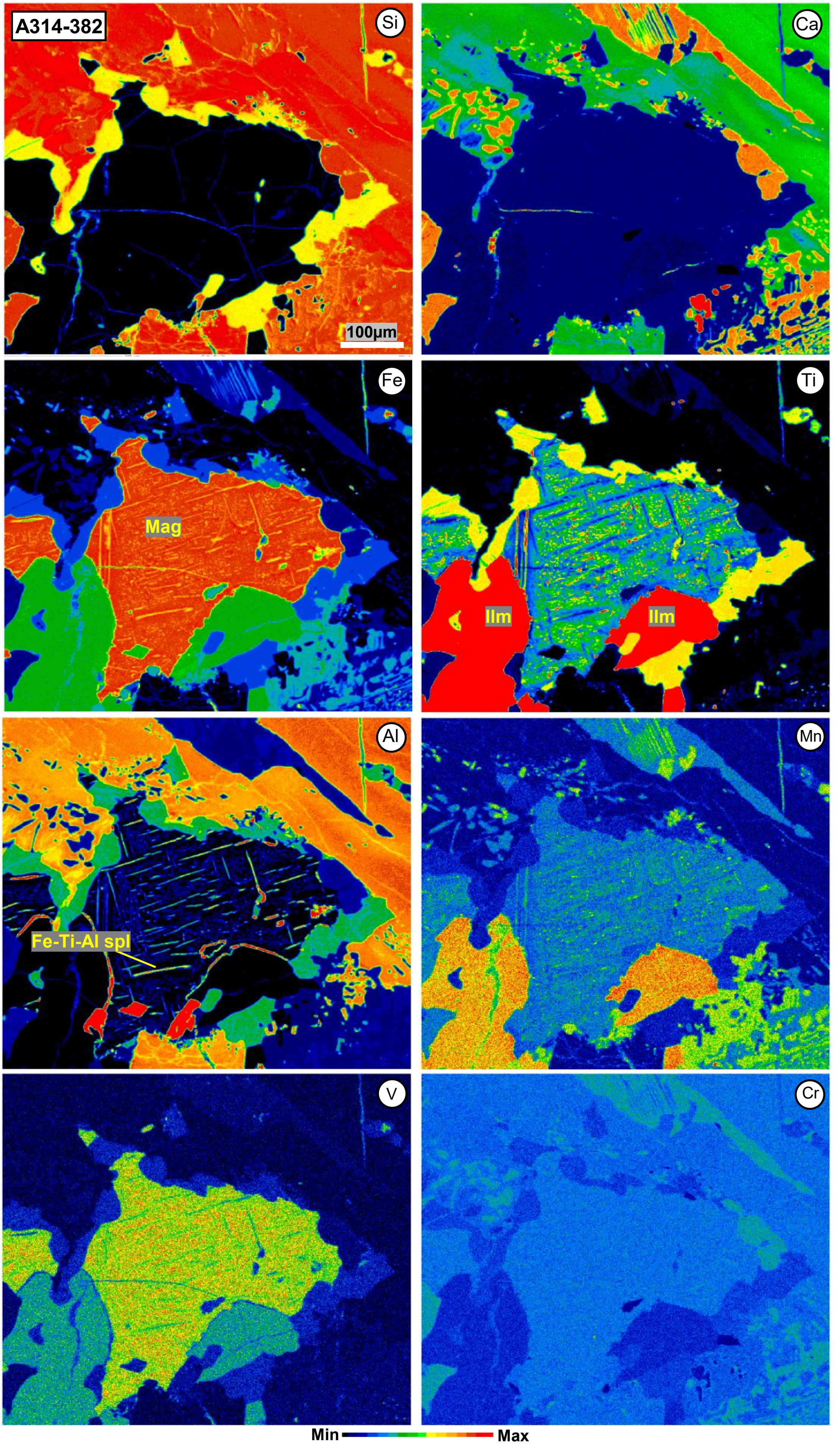

Supplementary Figure S3. Electron microprobe (EMP) wavelength-dispersive X-ray spectroscopy (WDS – Si, Ti, Al, Mn, V) and energy dispersive X-ray spectroscopy (EDS – Ca, Fe, Cr) element maps of magnetite showing the relative intensity of each element in sample A314-382. Elements, such as Fe, Al, Mn, V and Cr appear relatively homogeneously distributed throughout magnetite grains, whereas Ti shows diffuse zoning and depletions surrounding exsolution lamellae, which are composed of Fe-Ti-Al-spinel (Spl). Ilm: Ilmenite.

Supplementary Figure S4

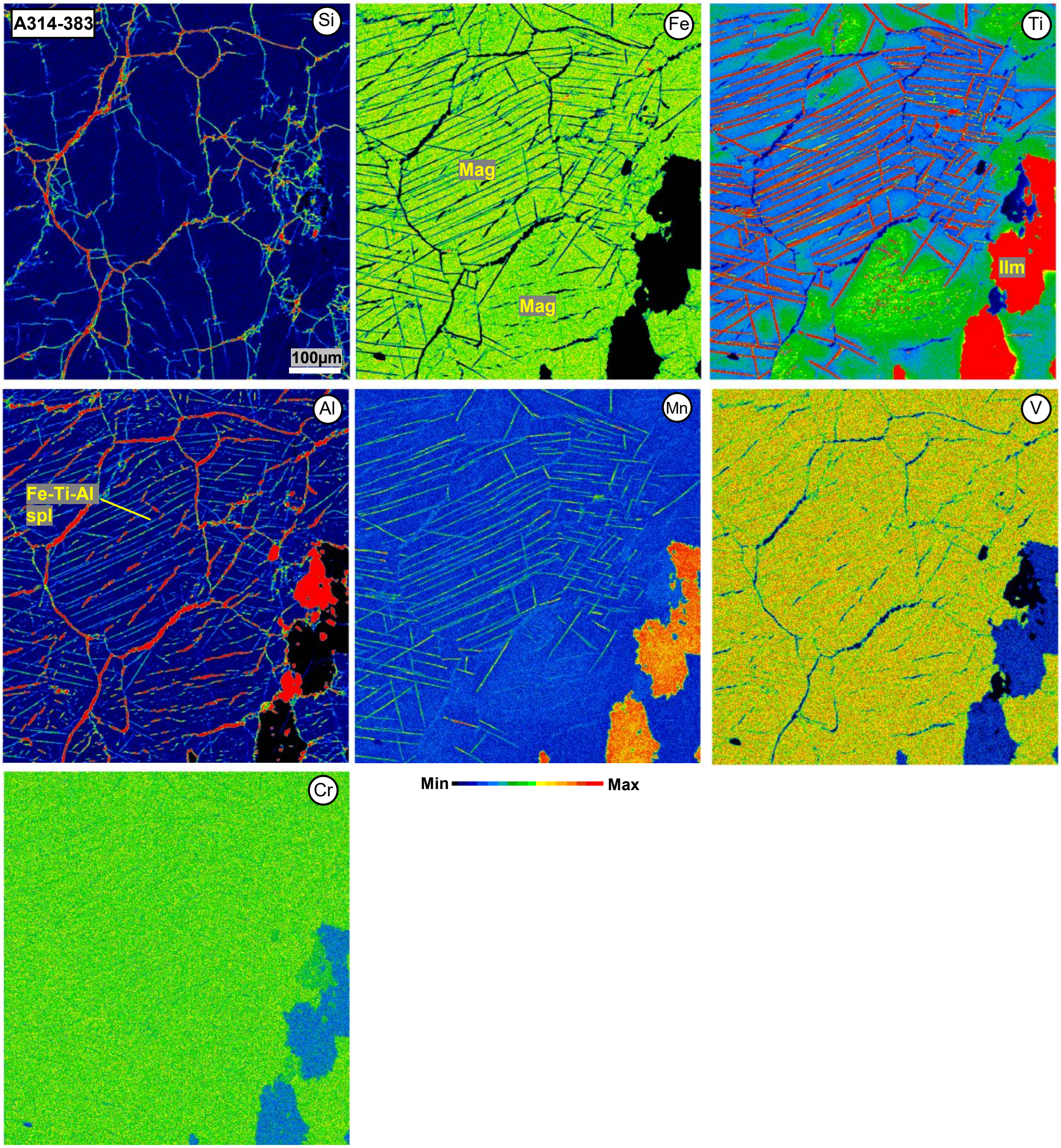

Supplementary Figure S4. Electron microprobe (EMP) wavelength-dispersive X-ray spectroscopy (WDS – Si, Ti, Al, Mn, V) and energy dispersive X-ray spectroscopy (EDS – Ca, Fe, Cr) element maps of magnetite showing the relative intensity of each element in sample A314-383. Elements, such as Fe, Al, Mn, V and Cr appear relatively homogeneously distributed throughout magnetite grains, whereas Ti shows diffuse zoning and depletions surrounding exsolution lamellae, which are composed of Fe-Ti-Al-spinel (Spl). Ilm: Ilmenite.

Supplementary Figure S5

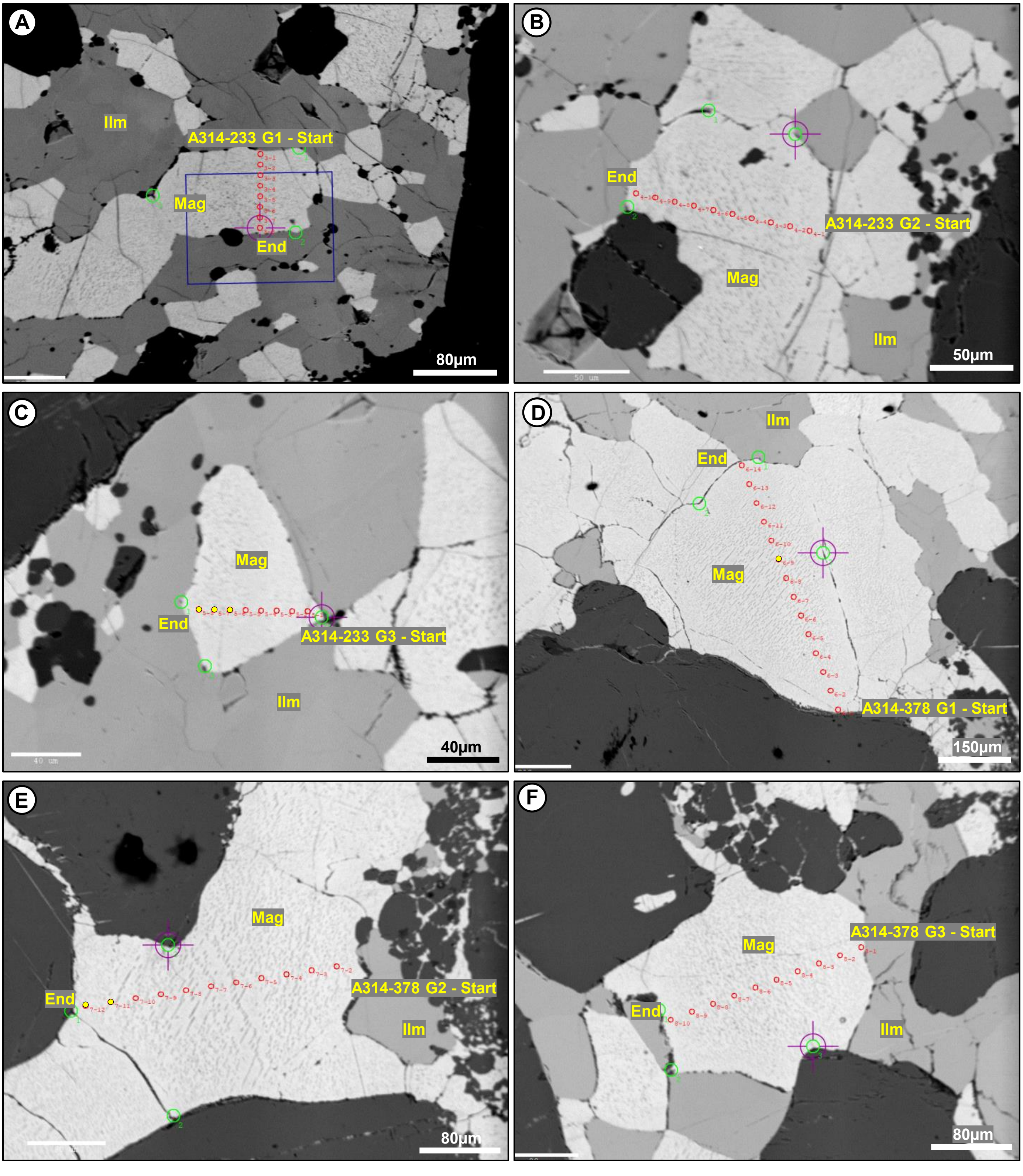

Supplementary Figure S5. Back-scatter electron (BSE) scanning electron microscope (SEM) images of EMP spot traverses in samples (A – C) A314-233, (D – F) A314-378. Corresponding EMP compositions for each datapoint are presented in Supplementary Table S6. Datapoints marked by a yellow circle indicate accidental non-magnetite species analysed (e.g., surrounding matrix, exsolution lamellae – i.e., clusters of parallel align Fe-Ti-Al-spinel in magnetite). Magnetite (Mag), Ilmenite (Ilm).

Supplementary Figure S6

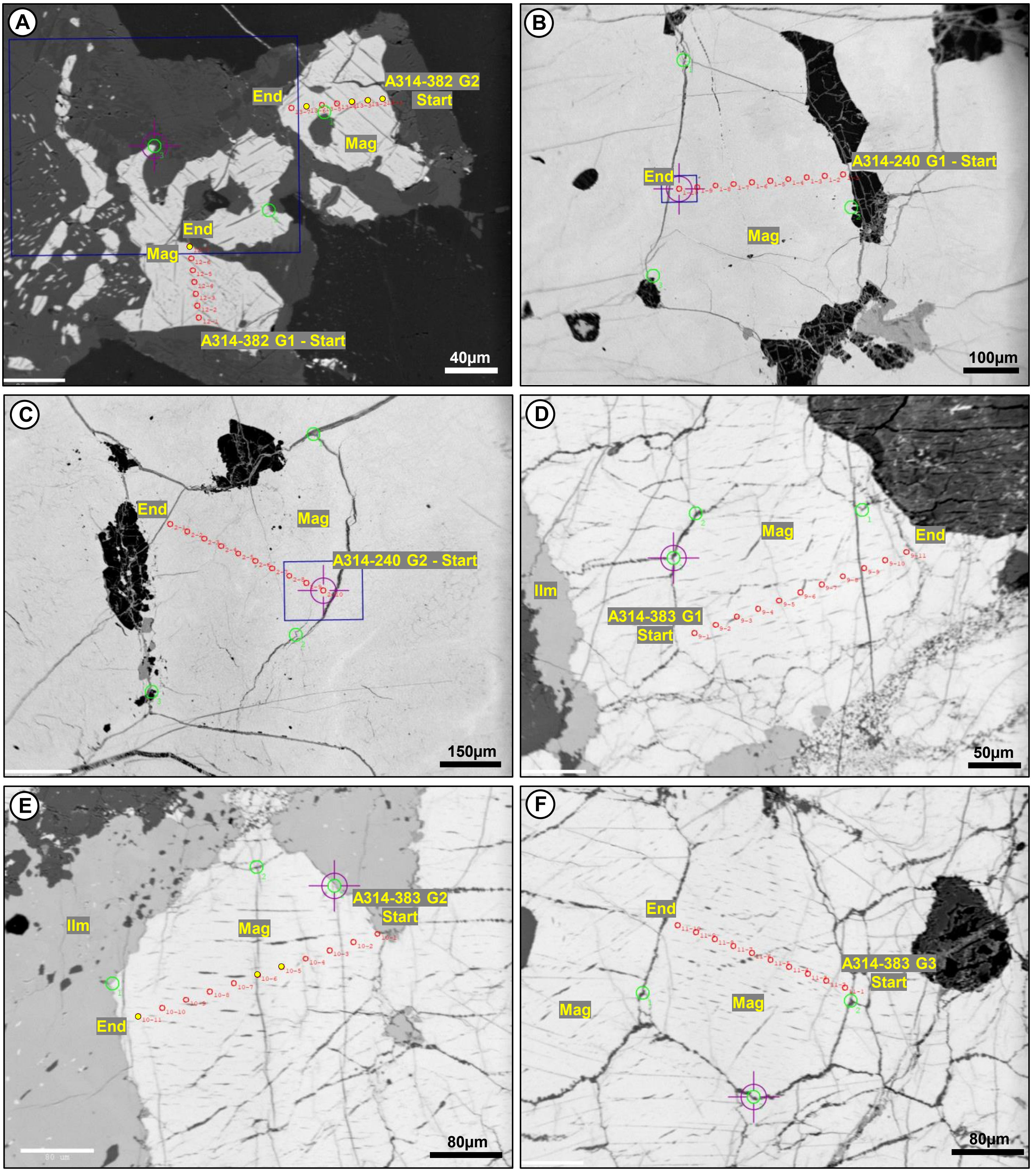

Supplementary Figure S6. Back-scatter electron (BSE) scanning electron microscope (SEM) images of EMP spot traverses in samples (A) A314-382, (B – C) A314-240, (D – F) A314-383. Corresponding EMP compositions for each datapoint are presented in Supplementary Table S6. Datapoints marked by a yellow circle indicate accidental non-magnetite species analysed (e.g., surrounding matrix, exsolution lamellae – i.e., clusters of parallel align Fe-Ti-Al-spinel in magnetite). Magnetite (Mag), Ilmenite (Ilm).

Supplementary Figure S7

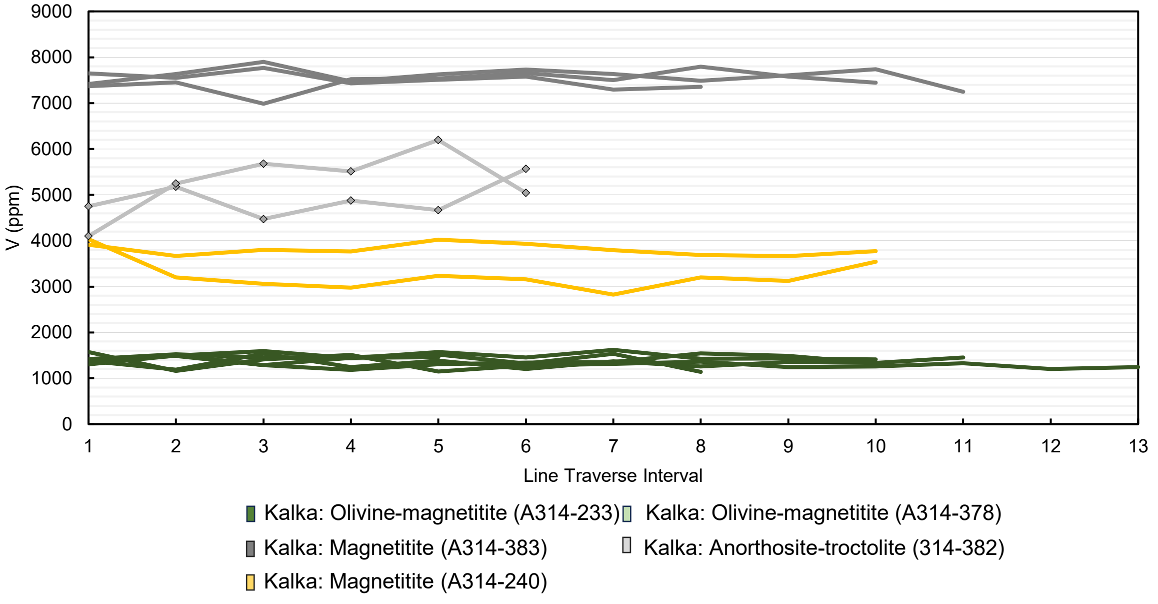

Supplementary Figure S7. Magnetite EMP spot traverse vs. vanadium (ppm) for analyses from samples A314-233, -378, -383, -382 and -240. The full dataset of EMP datapoints can be found in Supplementary Table S6.

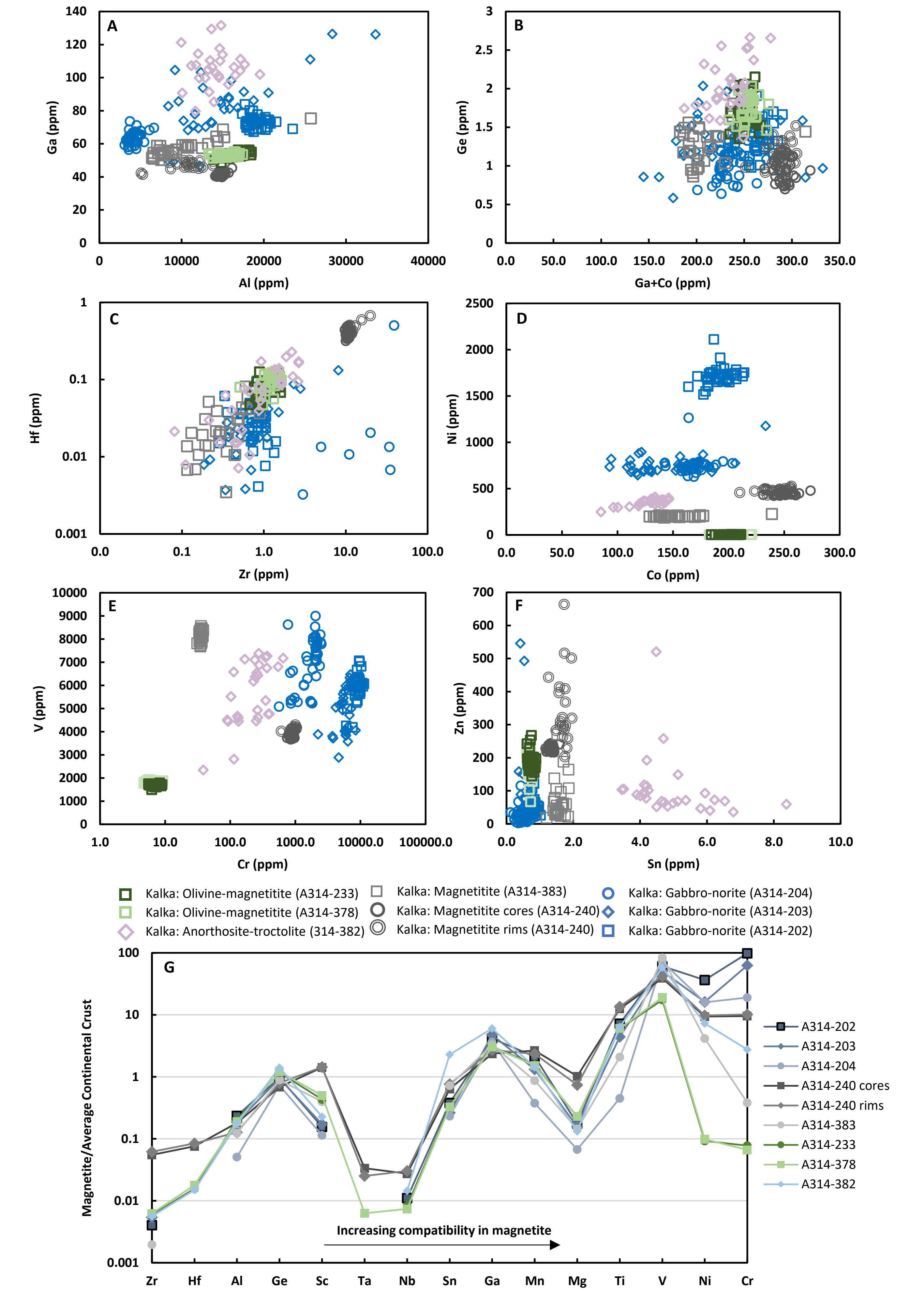

Supplementary Figure S8. (A – F) Bi-variate mineral LA-ICP-MS composition plots of trace element compositions of magnetite from Kalka lithologies. (G) Average continental crust normalised (after Rudnick and Gao, 2003) patterns for average LA-ICP-MS compositions of magnetite from Kalka lithologies, arranged in order of increasing compatibility (after Dare et al., 2014). The full dataset can be found in Supplementary Table S7.

Supplementary Figure S9

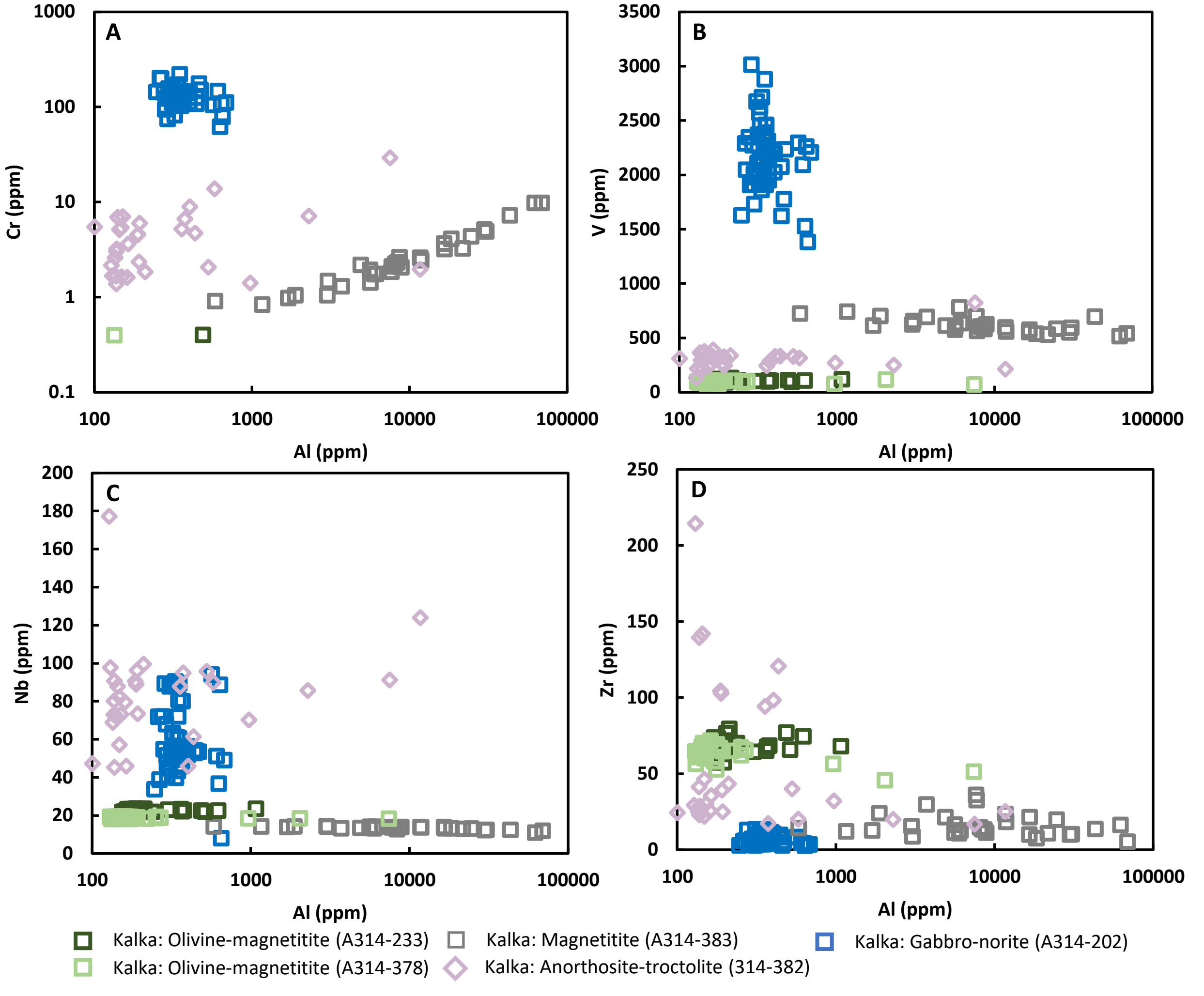

Supplementary Figure S9. (A – D) Bi-variate mineral LA-ICP-MS composition plots of trace element compositions of ilmenite from Kalka lithologies. The full dataset can be found in Supplementary Table S9.

Supplementary Figure S10

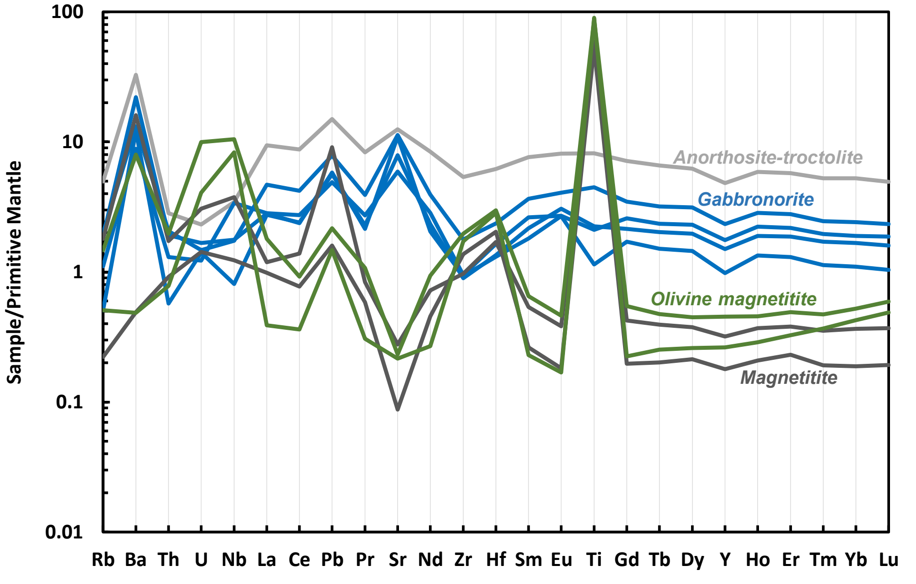

Supplementary Figure S10. Primitive mantle normalised (after Sun and McDonough, 1995) trace element patterns of Kalka whole-rock samples: Gabbronorite (A314-200, -202, -203, -204), Magnetitite (A314-240, 383), Olivine-Magnetitite (A314-233, -378), and Anorthosite-Troctolite (A314-382).

Supplementary Figure 11

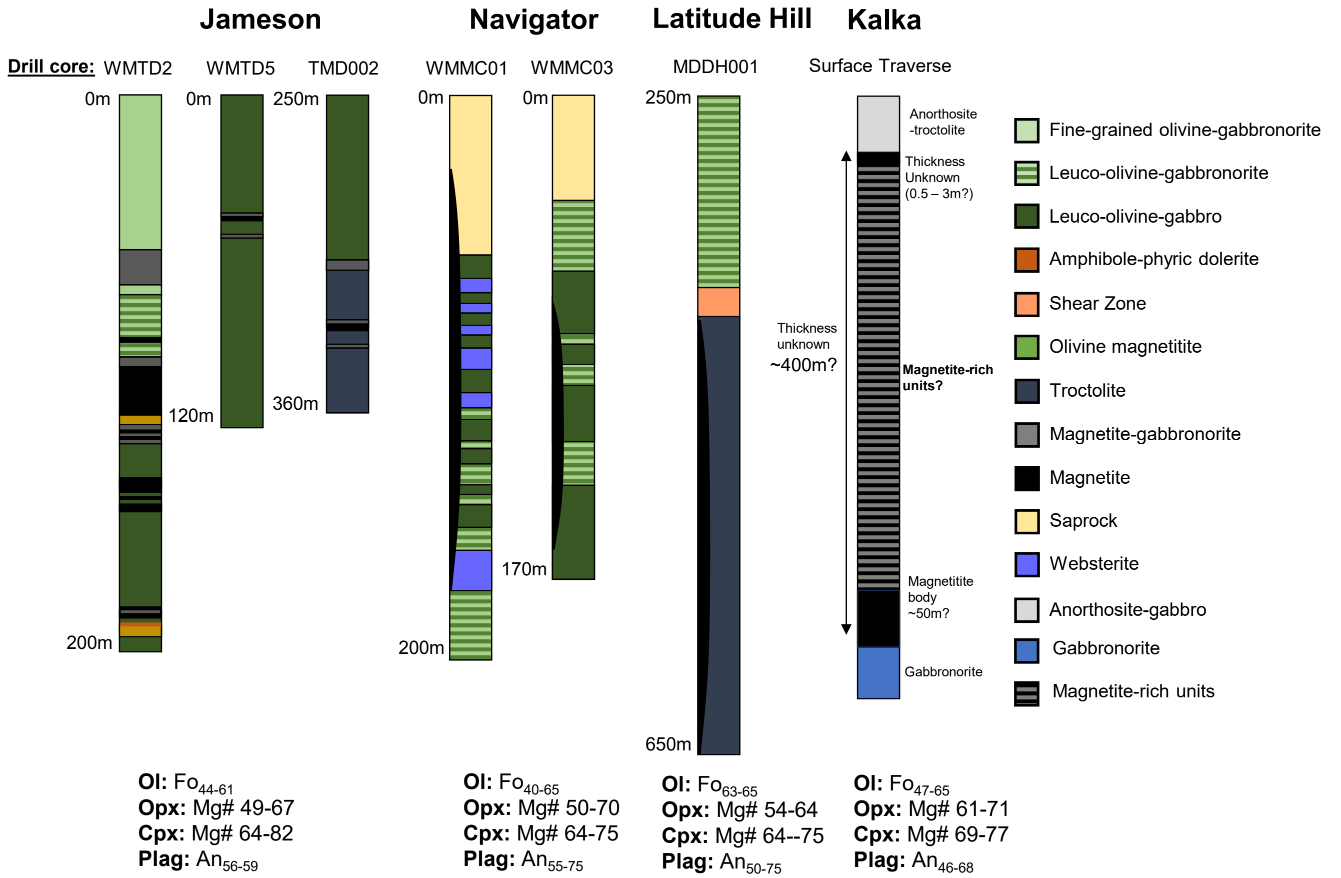

Supplementary Figure S11. Comparisons of drill core stratigraphic logs from Jameson, Navigator and Latitude Hill showing magnetitite occurrences and their adjacent lithologies (modified from Karykowski et al. (2017) and Polito et al. (2017)) compared with the inferred stratigraphic log of Kalka (this study – Figure 9). The compositional ranges of forsterite (Fo. mol.%) of olivine (Ol), Mg# of orthopyroxene (Opx) and clinopyroxene (Cpx), and plagioclase anorthite-content (An) for these stratigraphic logs are given for comparison (see Ballhaus and Glikson, 1995; Karykowski et al., 2016; Maier et al., 2014; Polito et al., 2017).

Supplementary Figure 12

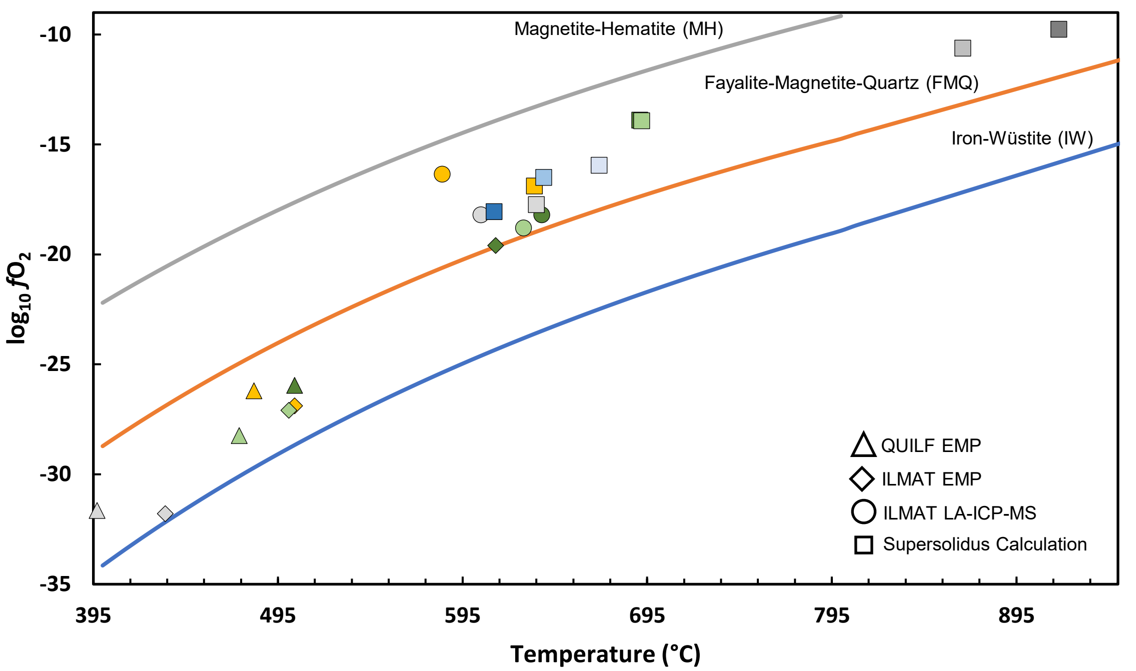

		A314-382	A314-233	A314-378	A314-383	A314-240-C	A314-240-R	A314-202	A314-203	A314-204
Subsolidus (magnetite-ilmenite paris)										
QUILF EMP	Temp (°C)	482	504	474	397					
	$\log_{10} fO_2$	-26.21	-25.97	-28.25	-31.66					
	ΔFMQ	-8.42	-2.73	-3.61	-2.98					
ILMAT EMP	Temp (°C)	504	613	501	434					
	$\log_{10} fO_2$	-26.9	-19.6	-27.1	-31.8					
	ΔFMQ	-3.36	-0.07	-3.45	-5.09					
ILMAT LA-ICP-MS	Temp (°C)	584	638	628	605					
	$\log_{10} fO_2$	-16.36	-18.2	-18.8	-18.2					
	ΔFMQ	4.18	0.63	0.36	1.61					
Supersolidus (magnetite)										
Canil and Lacourse (2020)	Temp (°C)	634	691	692	635	866	918	669	639	612
	$\log_{10} fO_2$	-16.89	-13.89	-13.92	-17.73	-10.62	-9.76	-15.95	-16.49	-18.05
Toplis and Corgne (2002)	ΔFMQ	2.04	3.40	3.35	1.17	2.68	2.57	1.95	2.29	1.57

Supplementary Figure S12. Oxygen fugacity (logfO2; ΔFMQ) vs. temperature (°C) plot calculated for: (i) subsolidus conditions using co-existing magnetite-ilmenite pairs from Fe-Ti oxide magnetitite units (A314-383, -233, -378) and troctolite-anorthosite unit (A314-382). Calculations were carried out using the ILMAT spreadsheet (Lepage, 2003) using the geothermobarometer by Spencer and Linsley (1981), and QUILF (Andersen et al., 1983). (ii) supersolidus conditions of magnetite using the TMg thermometer by Canil and Lacourse (2020) and experimental calibration of Toplis and Corgne (2002; see also Pang et al. (2010) and Wang et al. (2023)), the relationship between V partitioning and fO2 during supersolidus crystallisation (see text) for the sample samples, as well as A314-240 cores (C) and rims (R), and A314-202 – 204.

Supplementary Figure 13

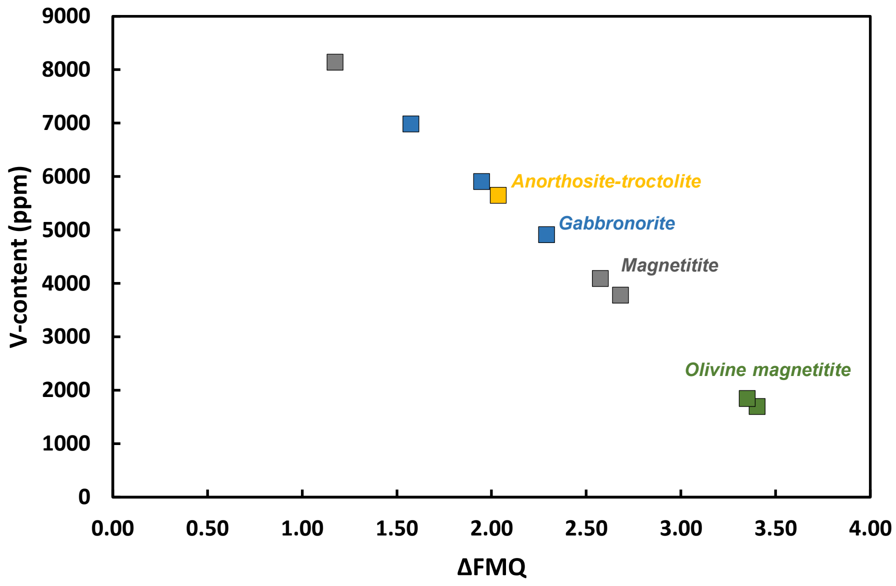

Supplementary Figure S13. Oxygen fugacity (ΔFMQ) vs. V-content (ppm) for magnetite crystallisation using the experimental calibration of Toplis and Corgne (2002 – see text for details).